Optics Letters

High-resolution wavefront shaping with a photonic crystal fiber for multimode fiber imaging

Lyubov V. Amitonova,[1,*] Adrien Descloux,[1,2] Joerg Petschulat,[2] Michael H. Frosz,[3] Goran Ahmed,[3] Fehim Babic,[3] Xin Jiang,[3] Allard P. Mosk,[1] Philip St.J. Russell,[3] and Pepijn W. H. Pinkse[1]

[1]Complex Photonic Systems (COPS), MESA + Institute for Nanotechnology, University of Twente, PO Box 217, 7500 AE Enschede, The Netherlands
[2]Carl Zeiss AG, Corporate Research and Technology, Carl Zeiss Promenade 10, 07749 Jena, Germany
[3]Max Planck Institute for the Science of Light, Guenther-Scharowsky Str. 1, 91058 Erlangen, Germany
*Corresponding author: l.amitonova@utwente.nl

Received 7 December 2015; revised 20 December 2015; accepted 20 December 2015; posted 23 December 2015 (Doc. ID 254852); published 29 January 2016

We demonstrate that a high-numerical-aperture photonic crystal fiber allows lensless focusing at an unparalleled resolution by complex wavefront shaping. This paves the way toward high-resolution imaging exceeding the capabilities of imaging with multi-core single-mode optical fibers. We analyze the beam waist and power in the focal spot on the fiber output using different types of fibers and different wavefront shaping approaches. We show that the complex wavefront shaping technique, together with a properly designed multimode photonic crystal fiber, enables us to create a tightly focused spot on the desired position on the fiber output facet with a subwavelength beam waist.

OCIS codes: (060.0060) Fiber optics and optical communications; (060.2350) Fiber optics imaging; (060.5295) Photonic crystal fibers; (060.2370) Fiber optics sensors.

http://dx.doi.org/10.1364/OL.41.000497

Integration of advanced fiber-optic components with cutting-edge approaches in optical imaging provides a powerful platform for micro-endoscopy, improving imaging resolution, field of view, and probe miniaturization. Standard single-mode and multimode optical fibers offer a very efficient and robust tool to look inside the human body in a minimally invasive way [1], for example, for optical studies of brain functions [2]. Multimode fibers also offer an attractive platform for high-dimensional quantum information processing [3]. Fiber bundles constructed from thousands of individual cores allow deep-tissue lensless imaging by using each core as a single pixel [4]. However, fiber bundles suffer from a limited imaging resolution and low fill factors dictated by the diameters of the individual fiber cores and the distances between the fibers. With the advent of complex wavefront shaping techniques, in which light is focused through a scattering medium using spatial light modulators (SLMs) [5–8], standard multimode (MM) optical fibers can now also be used for lensless fiber imaging [9–11]. Multimode fibers potentially offer imaging with a better resolution and a minimal cross section, compared to the fiber-bundle approach, by utilizing and controlling the high number of transverse fiber modes [12]. Recent works demonstrate possibilities for high-speed lensless fiber imaging by exploiting MM fiber and wavefront shaping techniques [13,14].

The resolution of multimode fiber imaging methods is fundamentally limited by the numerical aperture (NA) of the fiber probe. However, to make a fiber with a large NA, materials with widely different refractive indices should be used for the core and the cladding. Unfortunately, the range of indices available in transparent solids is relatively small. In practice, for a core of silica glass, NAs above 0.4 are very uncommon [15]. Nevertheless, high-resolution imaging in endoscopic format is extremely useful for numerous applications in the life sciences. State-of-the-art fiber imaging methods based on GRIN lenses, as well as methods based on fiber bundles, have a resolution of no better than 2 μm [16,17]. On the other hand, experimentally demonstrated beam waists on the output fiber facet in lensless multimode fiber imaging techniques vary from 1 to 2 μm [18–21]. Recently, several methods to improve the resolution further have been demonstrated [22,23]. These methods are based on using a high scattering medium, together with a multimode fiber, to increase the NA of the fiber. A resolution of up to 1.25 μm was demonstrated with such an approach [23]. It was also shown that a beam waist smaller than 1 μm could be achieved [22], but requires a high scattering medium to be fixed on a distance more than 200 μm from the fiber output, complicating endoscopic applications of such a fiber probe.

Microstructured optical fibers, also referred to as photonic crystal fibers (PCFs) [24,25], provide a unique tool for engineering specific fiber-optic interrogation protocols. Fibers of this class can have a substantially higher signal collection efficiency [26] than conventional fibers and offer promising solutions for realization of nonlinear optical fiber endoscopes [27,28]. PCFs with a properly tailored fiber structure offer a NA of more than 0.5 in the visible wavelength range [15].

Here we demonstrate that appropriately designed PCFs are well suited for lensless multimode fiber imaging at an

unprecedented resolution. We characterize and analyze the focal spot on the multimode fiber output of different fibers, as a function of the NA of the fiber and the number of controlled channels in a wavefront shaping procedure. We show that the beam waist depends only on the NA of the fiber, whereas the signal-to-noise ratio varies with the number of controlled channels on the SLM. Our experiments demonstrate that the complex wavefront shaping technique, together with a properly designed multimode PCF probe, enables a tightly focused spot on the desired position on the fiber output facet with a slightly subwavelength beam waist.

Our experiments are performed on a set of different step-index multimode fibers, as well as on multimode PCFs, with core diameters varying from 17 to 400 μm and a NA from 0.22 to 0.61. The length of each of the fibers is 12 cm. We use the continuous-wave linearly polarized output of a He–Ne laser with a wavelength of 633 nm. The experimental setup is presented in Fig. 1. A single-mode fiber is used to clean the laser mode, and its output is expanded to match the surface of our spatial light modulator. To control phase and amplitude on the input facet of the fiber with high speed, we use a 1920 × 1200 Vialux V4100 DMD. Lenses L1 and L2 are placed in a $4f$ configuration to image the phase mask on the back focal plane of a 40 × (NA = 0.65) objective that couples the light into the MM fiber. To modulate the high-spatial-frequency modes of the multimode fiber, objective 1 has to have a higher NA than the NA of the used fiber. Control of the higher-order modes of the fiber is critical to get a diffraction-limited focus for high NA fibers. A pinhole in the Fourier plane blocks all the diffraction orders, except the first, encoding the desired phase distribution. A 40 × objective (NA = 0.65) is used to collect light from the fiber output. Two cameras image both the input and the output facets of the MM fiber in a polarization-insensitive way.

The complex wavefront-shaping algorithm to create the tightly focused laser spot on the fiber output is as follows. Each mirror of the DMD can be set to two different tilt angles, therefore creating a binary amplitude mask. By controlling the tilt of every mirror, 2D blazed gratings can be created. With an appropriately tilted input light field, the diffracted light propagates along the normal of the DMD surface (see Fig. 1). An unoptimized plane wave that is incident on the fiber input gives rise to a speckle pattern on the output fiber facet. We divide the DMD area into a number of superpixels (segments) and modulate the phase of each superpixel by shifting the grating pattern over 2π in three steps. All other superpixels are used as references. The phase that leads to the highest intensity in the desired spot on the fiber output for every superpixel is kept. As a result, the intensity on the target is enhanced relative to the uncontrolled initial speckle. The time required for our optimization procedure is limited by the frame rate of the camera we used and is 150 ms for each superpixel. As a result, the whole optimization procedure takes from several seconds to 2.5 min, depending on the number of superpixels that we control.

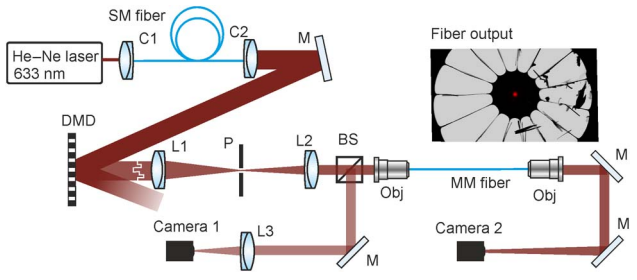

Fig. 1. Experimental setup (MM, multimode fiber; DMD, digital micromirror device; SM, single-mode fiber; M, mirrors; L, lenses; BS, beam splitter; Obj, objectives).

The typical beam waist of the focal spot on the output facet of a normal MM fiber after the optimization procedure is more than 1 μm [18–21]. In contrast, for photonic crystal fibers, the spot is smaller than the optical wavelength. Due to the high contrast between the silica core and the air cladding, the numerical aperture of such a fiber is higher than that of standard step-index fibers [15]. Photonic crystal fibers for our experiments were fabricated using the stack-and-draw technique [29]. By careful control of the pressure applied to the cladding during drawing, samples with different core diameters and wall thicknesses could be obtained from the same preform. The scanning electron micrographs of PCFs that we used are shown in Figs. 2(a) and 2(b), and Figs. 3(a) and 3(b). For all PCFs, we follow the optimization procedure described above to create a tightly focused spot on the output facet near the core axis.

First, we examine two PCFs with the same type of hexagonal structure consisting of six large air holes, but with different thicknesses of the suspending webs, as can be seen in Figs. 2(a) and 2(b). The results of the wavefront shaping procedure for these fibers are presented in Figs. 2(c) and 2(d). Our measurements show that the width of the suspending webs is crucial for creating a high NA fiber probe and achieving a small beam waist of the focused spot on the fiber output. Despite a high refractive index contrast between the silica and air, the photonic crystal fiber with a 1.3 μm thick web only allows to focus 633 nm of light down to a full-width at half-maximum (FWHM) of 1.38 ± 0.01 μm, which corresponds to a numerical aperture NA = 0.23 for our wavelength. The focal spot is shown in Fig. 2(c). This does not provide any gain in resolution compared to the standard commercially available step-index silica fibers. However, for the PCF with a very similar profile structure but with a width of the suspending webs $w = 255$ nm, a FWHM of the focal spot 0.62 ± 0.01 μm can be achieved.

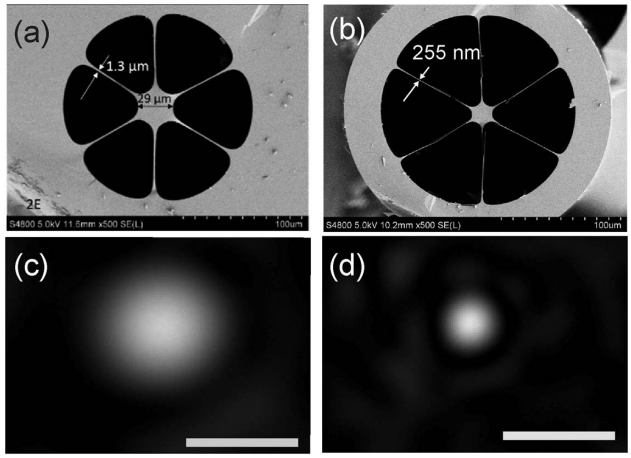

Fig. 2. Profiles of a PCF with core diameter ∅ 29 μm and width of the suspending webs $W = 1.3$ μm (a) and a PCF with ∅ 16.8 μm and $w = 255$ nm (b), and corresponding fiber outputs after wavefront shaping with NA ≈ 0.23 (c) and NA ≈ 0.51 (d). Scale bars are 100 μm (a), (b) and 2 μm (c), (d).

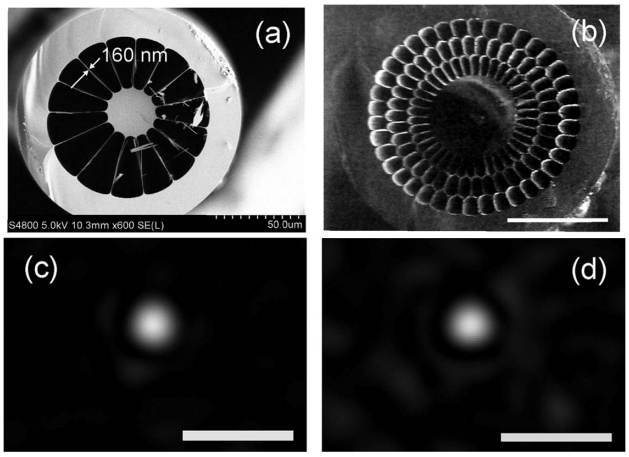

Fig. 3. Profiles of the PCF with a round core shape with a diameter ∅ 28 μm and width of the suspending webs $w = 160$ nm (a) and with a diameter ∅ 45 μm and width of the suspending webs $w = 290$ nm (b), and corresponding fiber outputs after wavefront shaping with NA ≈ 0.59 (c) and NA ≈ 0.61 (d). Scale bars are 50 μm (a), (b) and 2 μm (c), (d).

This corresponds to a numerical aperture of 0.51 and already allows imaging in endoscopic format with a resolution higher than is provided by standard step-index silica fibers. The corresponding fiber output is shown in Fig. 2(d).

In a second set of experiments, we examine the parameters of the focal spot on the PCF output after the wavefront shaping procedure, for two different types of PCF structures. The first structure we have chosen consists of 15 large air holes, which are organized to create a nearly round core shape presented in Fig. 3(a). The thickness of the suspending webs for this fiber is only 160 nm. The second structure (commercially purchased from Fiberware, Germany) consists of a large number of air holes, which are organized in three rows around the fiber core to create a round core shape, as shown in Fig. 3(b). The thickness of the suspending webs of $w = 290$ nm is comparable with the one we used in the first set of measurements. These fiber structures do not have hexagonal features which could lead to losses of higher-order modes and, thereby, effectively decrease the NA.

The results of the wavefront shaping procedure performed on PCFs with different structures are shown in Figs. 3(c) and 3(d). For the PCF presented in Fig. 3(a), we achieve a FWHM of the focal spot equal to 0.54 ± 0.01 μm. This corresponds to a numerical aperture of about 0.59 for our wavelength. The focal spot on the output of this fiber is shown in Fig. 3(c). For the second PCF, with a cladding structure consisting of a large number of air holes organized in three concentric rings around the fiber core, we achieve a FWHM of the focal spot of 0.52 ± 0.01 μm, which corresponds to a numerical aperture of more than 0.6 for our wavelength. The fiber output after wavefront shaping is shown in Fig. 3(d). Both of these PC fibers allow high-resolution imaging in endoscopic format. As our experiments show, the smallest focus is achieved with the PCF from Fig. 3(b), with a close second achieved with the PCF from Fig. 3(a).

In a third set of experiments, we examine the properties of the focused fiber spot as a function of the number of controlled channels (patches or superpixels) on the DMD for three different standard step-index fibers with an NA from 0.22 to 0.48 and core diameters from 50 to 400 μm, according to their specifications (Thorlabs), and for two high NA PCFs with profiles presented in Figs. 2(b) and 3(b). For every fixed number of channels, we repeat the optimization procedure described above five times for different spot positions near the fiber core axis to obtain several characterizing parameters of the focal spot and their standard deviation. To retrieve the FWHM diameter, we fit the resulting spot with a Gaussian function. The second parameter that we investigate is the fraction of the power in the focus. We define the relative power in the focal spot as $\gamma^2 = P_f/P_0$, where P_f is the power in the focus area with a center corresponding to that of the focal spot and a diameter equal to the FWHM of the Gaussian spot. P_0 is the total power on the fiber output which, in an ideal fiber, is not changed by wavefront shaping.

Experimental results are presented in Fig. 4. The power in the focal spot, γ^2 in percent, and the FWHM diameter of the Gaussian spot as a function of the number of controlled channels is presented in Figs. 4(a) and 4(b), respectively. Symbols represent experimental data for five different fiber probes: a step-index fiber with a core diameter of 50 μm and NA = 0.22 (green filled circles); a step-index fiber with a core diameter of 300 μm and NA = 0.39 (blue open circles); a step-index fiber with a core diameter of 400 μm and NA = 0.48 (violet filled triangles); a PC fiber with a core diameter of about 16.8 μm and NA ≈ 0.51 (red filled asterisks); and a PC fiber with a core diameter of 45 μm and NA≈0.61 (green open asterisks).

It is well known that for phase-only wavefront shaping after optimization of the N-controlled incident channels, the power on the target spot can be enhanced relative to the uncontrolled initial speckle by a factor of $\eta = 1 + (N - 1)\pi/4$ [5]. Here the enhancement is defined as $\eta = P_{f1}/P_{f0}$, where P_{f1} is the power in the focal spot after optimization, and P_{f0} is the average power in the focal spot before optimization. Consequently, the ratio between the enhancement and power in the focus is given by $\eta = \gamma^2 r_0^2/r_f^2$, where r_0 is the radius of the fiber core

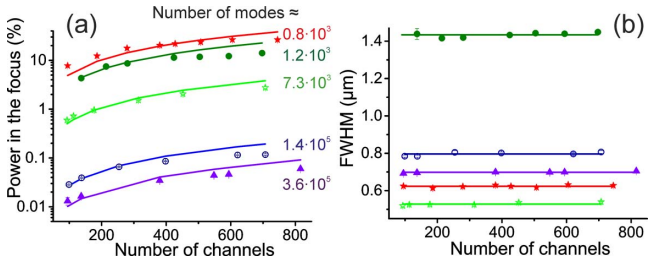

Fig. 4. Power fraction in the focal spot γ^2 in percent (a) and the FWHM diameter of the Gaussian spot (b) as a function of the number of controlled channels on the DMD. The dots represent experimental data for four different fiber probes: three step-index fibers with core diameter ∅ 50 μm and NA = 0.22 (green filled circles), ∅ 300 μm and NA = 0.39 (blue open circles), and ∅ 400 μm and NA = 0.48 (violet filled triangles); and two PCFs with core diameter ∅ 16.8 μm and NA about 0.51 (red filled asterisks) and ∅ 45 μm and NA about 0.61 (green open asterisks). The error bars are smaller than the symbols. The solid lines in (a) represent the theoretical calculated γ^2 for fibers with a round core shape. The numbers in (a) represent the approximate number of modes for each fiber.

and r_f the radius of the focal spot. For a diffraction limited spot $r_f = \lambda/(4\mathrm{NA})$ and the enhancement $\eta = 4V^2/\pi^2\gamma^2$, where $V = 2\pi r_0 \mathrm{NA}/\lambda$ is the V-parameter of the fiber. The coefficient $4V^2/\pi^2$ is approximately equal to the number of modes (N_{modes}) in a multimode cylindrical fiber waveguide.

As a result, $\gamma^2 = 0.5[1 + (N - 1)\pi/4]/N_{\mathrm{modes}}$, where the 0.5 accounts for the fact that in our experiments we control only one polarization on the fiber input. Theoretical predictions are presented in Fig. 4(a) as solid lines with corresponding colors. As can be seen from Fig. 4(a), the power in the focus continuously grows, increasing more than three times for each fiber with an increase in the number of controlled channels from 100 to 700. It is interesting that for the same number of segments the power in the focus is significantly smaller for fibers with more modes. Theoretical calculations are in good agreement with the experimental data, especially in the area of a small number of channels. Deviations from the ideal conditions are caused by noise, as well as the difference between the number of segments controlled by the DMD and the number of actually controlled modes of the fiber. This reduces the experimentally measured enhancement for a high number of controlled channels [30].

In contrast, the size of the focal spot was found not to depend on the number of controlled channels and remains constant within 3% for every fiber that we use, as can be seen in Fig. 4(b). As a result, the resolution of lensless multimode fiber imaging will not depend on the number of segments one controls with the SLM. Nevertheless, for imaging with a higher signal-to-background ratio, the number of controlled channels should be increased. As can be seen from our experimental data and the formula derived above, multimode fiber imaging shows a negative dependence between field of view (i.e., the fiber core diameter) or resolution (fiber NA) and imaging contrast for a fixed number of controlled channels on the SLM. This property sets multimode fiber imaging apart from other standard microscope imaging techniques and should be taken into account. For example, for a fixed number of SLM pixels, an increase in the relative power in the tight focus on the fiber output requires a decrease in the core radius of the fiber probe.

To summarize, we examine different types of multimode fibers and demonstrate that an appropriately designed solid-core PCF can be employed for lensless multimode fiber imaging at an unparalleled resolution. We analyze the parameters of the focal spots on the multimode fiber output as a function of the number of controlled channels in a wavefront shaping procedure. We show that the signal-to-noise ratio significantly improves with an increasing number of controlled channels whereas, in contrast, the beam waist remains constant. Our experiments demonstrate that the wavefront shaping technique together with a properly designed multimode PCF probe enables the creation of a tightly focused subwavelength spot on a desired position on the fiber output facet with a beam waist of 0.52 μm at a wavelength of 633 nm.

Funding. Stichting voor Fundamenteel Onderzoek der Materie (FOM); Nederlandse Organisatie voor Wetenschappelijk Onderzoek (NWO); European Research Council (ERC) (279248); Stichting voor de Technische Wetenschappen (STW).

Acknowledgment. The authors thank Sergei Sokolov, Cornelis Harteveld, and Willem Vos for support and discussions.

REFERENCES

1. B. A. Flusberg, E. D. Cocker, W. Piyawattanametha, J. C. Jung, E. L. M. Cheung, and M. J. Schnitzer, Nat. Methods **2**, 941 (2005).
2. L. V. Doronina-Amitonova, I. V. Fedotov, O. I. Ivashkina, M. A. Zots, A. B. Fedotov, K. V. Anokhin, and A. M. Zheltikov, J. Biophotonics **3**, 660 (2010).
3. H. Defienne, M. Barbieri, I. A. Walmsley, B. J. Smith, and S. Gigan, "Control of two-photon quantum walk in a complex multimode system by wavefront shaping," arXiv 1504.03178 (2015).
4. L. V. Doronina-Amitonova, I. V. Fedotov, O. Efimova, M. Chernysheva, A. B. Fedotov, K. V. Anokhin, and A. M. Zheltikov, Appl. Phys. Lett. **101**, 233702 (2012).
5. I. M. Vellekoop and A. P. Mosk, Opt. Lett. **32**, 2309 (2007).
6. I. M. Vellekoop, A. Lagendijk, and A. P. Mosk, Nat. Photonics **4**, 320 (2010).
7. J. Jang, J. Lim, H. Yu, H. Choi, J. Ha, J.-H. Park, W.-Y. Oh, W. Jang, S. Lee, and Y. Park, Opt. Express **21**, 2890 (2013).
8. Y. M. Wang, B. Judkewitz, C. A. DiMarzio, and C. Yang, Nat. Commun. **3**, 928 (2012).
9. T. Čižmár and K. Dholakia, Opt. Express **19**, 18871 (2011).
10. T. Čižmár and K. Dholakia, Nat. Commun. **3**, 1027 (2012).
11. R. Di Leonardo and S. Bianchi, Opt. Express **19**, 247 (2011).
12. R. N. Mahalati, R. Y. Gu, and J. M. Kahn, Opt. Express **21**, 1656 (2013).
13. A. M. Caravaca-Aguirre, E. Niv, D. B. Conkey, and R. Piestun, Opt. Express **21**, 12881 (2013).
14. L. V. Amitonova, A. P. Mosk, and P. W. H. Pinkse, Opt. Express **23**, 20569 (2015).
15. W. J. Wadsworth, R. M. Percival, G. Bouwmans, J. C. Knight, T. A. Birks, T. D. Hedley, and P. St.J. Russell, IEEE Photonics Technol. Lett. **16**, 843 (2004).
16. K. K. Ghosh, L. D. Burns, E. D. Cocker, A. Nimmerjahn, Y. Ziv, A. E. Gamal, and M. J. Schnitzer, Nat. Methods **8**, 871 (2011).
17. E. Laemmel, M. Genet, G. Le Goualher, A. Perchant, J.-F. Le Gargasson, and E. Vicaut, J. Vasc. Res. **41**, 400 (2004).
18. I. N. Papadopoulos, S. Farahi, C. Moser, and D. Psaltis, Opt. Express **20**, 10583 (2012).
19. Y. Choi, C. Yoon, M. Kim, T. D. Yang, C. Fang-Yen, R. R. Dasari, K. J. Lee, and W. Choi, Phys. Rev. Lett. **109**, 203901 (2012).
20. S. Bianchi and R. Di Leonardo, Lab Chip **12**, 635 (2012).
21. I. N. Papadopoulos, S. Farahi, C. Moser, and D. Psaltis, Biomed. Opt. Express **4**, 260 (2013).
22. I. N. Papadopoulos, S. Farahi, C. Moser, and D. Psaltis, Opt. Lett. **38**, 2776 (2013).
23. Y. Choi, C. Yoon, M. Kim, J. Yang, and W. Choi, Opt. Lett. **38**, 2253 (2013).
24. P. Russell, Science **299**, 358 (2003).
25. J. C. Knight, Nature **424**, 847 (2003).
26. M. T. Myaing, J. Y. Ye, T. B. Norris, T. Thomas, J. R. Baker, Jr., W. J. Wadsworth, G. Bouwmans, J. C. Knight, and P. St.J. Russell, Opt. Lett. **28**, 1224 (2003).
27. A. A. Lanin, I. V. Fedotov, D. A. Sidorov-Biryukov, L. V. Doronina-Amitonova, O. I. Ivashkina, M. A. Zots, C.-K. Sun, F. Ömer Ilday, A. B. Fedotov, K. V. Anokhin, and A. M. Zheltikov, Appl. Phys. Lett. **100**, 101104 (2012).
28. E. R. Andresen, G. Bouwmans, S. Monneret, and H. Rigneault, Opt. Express **21**, 20713 (2013).
29. J. C. Knight, T. A. Birks, P. St.J. Russell, and D. M. Atkin, Opt. Lett. **21**, 1547 (1996).
30. D. Akbulut, T. J. Huisman, E. G. van Putten, W. L. Vos, and A. P. Mosk, Opt. Express **19**, 4017 (2011).